The Astrophysical Journal, 997:204 (9pp), 2026 February 1 https://doi.org/10.3847/1538-4357/ae2756

Solar Orbiter's Passage through Comet Leonard's Tail while in the He^+ Focusing Cone

Bernard J. Vasquez[1], Charles W. Smith[1], Antoinette Galvin[1], Lynn Kistler[1], Lorna Ellis[1], Allison Swart[1], Timothy J. Stubbs[2], Kevin Delano[3,4], C. J. Owen[5], S. Livi[6,7], P. Louarn[8], S. T. Lepri[7], J. M. Raines[7], R. M. Dewey[7], B. L. Alterman[4], Yeimy J. Rivera[9], Erik Fischer[7], and Evan P. Shimoun[7]

[1] Space Science Center, University of New Hampshire, Durham, NH 03824, USA; bernie.vasquez@unh.edu
[2] NASA Goddard Space Flight Center, Solar System Exploration Division, Greenbelt, MD 20769, USA
[3] University of Maryland, Baltimore County, Baltimore, MD 21250, USA
[4] NASA Goddard Space Flight Center, Heliophysics Science Division, Greenbelt, MD 20769, USA
[5] Mullard Space Science Laboratory, Department of Space and Climate Physics, University College London, Holmbury St. Mary, Dorking, Surrey RH5 6NT, UK
[6] Space Science and Engineering, Southwest Research Institute, San Antonio, TX 78238, USA
[7] Department of Climate and Space Sciences & Engineering, University of Michigan, Ann Arbor, MI 48109, USA
[8] IRAP, Toulouse University, CNRS, CNES, Toulouse, France
[9] Center for Astrophysics, Harvard & Smithsonian, Cambridge, MA 02138, USA

Received 2025 September 3; revised 2025 November 19; accepted 2025 November 30; published 2026 January 23

Abstract

The Solar Orbiter spacecraft crossed Comet Leonard's ion tail on 2021 December 17 near 1 au. In and near the ion tail, significant amounts of singly charged oxygen (O^+) ions were detected by the Heavy Ion Sensor on board the spacecraft. These ions are likely the result of outgassed water molecules from the comet that became ionized and disassociated into protons and O^+ ions and that were then picked up by the interplanetary magnetic field and advected outward with the solar wind. At this time, the spacecraft was also located amidst the denser parts of the interstellar helium (He) neutrals that are focused here by their gravitational interaction with the Sun. Pickup He^+ ions in greater numbers are also found in this region and form when neutrals interact with solar photons. Newly ionized ions can generate waves that propagate mainly along the background magnetic field before the waves scatter the ions toward isotropy. Spectral magnetic field analyses are employed to find mainly elliptically polarized waves associated with O^+ and He^+ from ring-beam instabilities. Waves associated with He^+ are identified, but O^+ waves are not seen. Visibility is concluded to be affected by the relative amplitude of the waves to turbulence, and the visibility increases when the sampling direction is more aligned with the background magnetic field.

Unified Astronomy Thesaurus concepts: Pickup ions (1239); Interplanetary turbulence (830); Solar wind (1534); Comets (280)

1. Introduction

Comet Leonard (C2021/A1) was a long-period comet that reached perihelion on 2022 January 3. The orbit was highly inclined to the ecliptic plane, but in 2021 December in the middle of the month it crossed the ecliptic. It passed closest to Earth on December 12 at a separation distance of 0.23 au (S. R. Watson et al. 2024). Thereafter, the comet made a very close pass of Venus at a separation of only 0.02 au on December 18 (S. R. Watson et al. 2024). The comet was relatively inactive up to about December 13 and then underwent a number of outbursts (D. Jewitt et al. 2023; N. Biver et al. 2024). The gas originated from a nucleus of ∼0.5 km in diameter (D. Jewitt et al. 2023). The ion tail of this gas-rich comet showed a number of changes during the active phase, including streamers, kinks, and disconnection events associated with heliospheric current sheet crossings (S. Faggi et al. 2023; D. Jewitt et al. 2023; N. Biver et al. 2024; S. R. Watson et al. 2024, 2025). Ultimately, Comet Leonard broke apart in 2022 February (D. Jewitt et al. 2023).

The Solar Orbiter spacecraft passed through the tail of Comet Leonard between 2021 December 16 and 18 at a heliocentric distance of 1.01 au and about 0.25 au from the comet nucleus. Singly charged oxygen (O^+) was observed throughout this interval. This ion likely originated from the dissociation of water molecules outgassed from the comet that were then picked up by the interplanetary magnetic field when they acquired a charge. At the same time, Solar Orbiter was well within the focusing cone of neutral interstellar helium (He). From neutral He, interstellar singly charged helium (He^+) is produced mainly by extreme-ultraviolet (EUV) photons from the Sun. The concentration of He^+ is high within the focusing cone (C. Drews et al. 2012; D. J. Gershman et al. 2013; S. A. Spitzer et al. 2024) because the neutral He has a high concentration and also because the focusing cone is relatively near the Sun where the concentration of EUV photons (decreasing generally with the square of heliocentric distance) is also large.

Both O^+ and He^+ are injected with low velocities relative to the solar wind. As such, the newly ionized particles are unstable to a ring-beam instability that generates waves (M. A. Lee & W.-H. Ip 1987; B. T. Tsurutani 1991). Once ions become fully scattered by the waves, they no longer contribute to wave generation. The accumulation of additional wave power requires yet more newly ionized particles.

Using magnetic field power and polarization spectra, waves associated with He^+ have been occasionally detected near 1 au (M. R. Argall et al. 2015; M. K. Fisher et al. 2016). This low occurrence has been attributed to the presence of interplanetary turbulence, where the energy cascade draws off the energy associated with the pickup ion waves and limits the amount of energy that they can accumulate with time (B. E. Cannon et al. 2014a, 2014b). In an interval where the waves associated with He^+ can be observed, the opportunity to identify O^+-associated waves should be enhanced.

Spectral techniques common to the study of pickup ions from interstellar neutrals, especially in the outer heliosphere, are applied in the present analysis. Waves associated with He^+ are identified on December 16. Those intervals containing the He^+ did not show signs of O^+ waves. Waves associated with O^+ were not found in any other interval where the He^+ waves were absent during the tail crossing. Reasons why this could occur are discussed.

The outline of this paper is as follows: Section 2 describes the data and analysis methods. Results are presented in Section 3 and discussed in Section 4. Section 5 gives conclusions.

2. Data and Analysis Methods

Solar Orbiter data from 2021 December 16 to 2021 December 18 are used in this study. Magnetic field spectra to search for waves are obtained using magnetic field data at eight vectors per second that are publicly available at the Space Physics Data Facility website (T. S. Horbury et al. 2020). The magnetic field instrument on Solar Orbiter is a flux gate magnetometer. Plasma data are obtained from the Solar Wind Analyzer consisting of the Proton and Alpha Sensor (PAS) and the Heavy Ion Sensor (HIS) instrument suite (C. J. Owen et al. 2020; S. Livi et al. 2023). Background solar wind conditions are assessed with hourly proton data from PAS merged with hourly magnetic field data that are publicly available. The time-of-flight ion spectrometer HIS (S. Livi et al. 2023) provides species composition organized by energy per charge (E/Q), mass per charge (M/Q), and (under certain conditions) mass (M). For the present study, species are isolated principally through their M/Q. For the M/Q of 16, the oxygen (O^+) is well isolated from other species. For M/Q of four, measured species include helium (He^+), but also potentially solar wind magnesium (Mg^{+6}), silicon (Si^{+7}), sulfur (S^{+8}), and iron (Fe^{+14}). For this study, $M/Q = 4$ solar wind species that include energy measurements have been isolated out by their measured mass while the remainder of solar wind contributions (where only M/Q is available) are confined to solar wind speeds. The measurement cadence for HIS is 30 s, but for statistical reasons the measurements of pickup He^+ and O^+ ions shown in this paper are aggregated in counts per hour.

When a new pickup ion of species i is injected at low speed relative to the flow speed of the solar wind $V_{\rm SW}$, it streams along the background magnetic field $\boldsymbol{B}_0$ with a speed $\sim -V_{\rm SW}\cos\theta_{BV}$, where θ_{BV} is the angle between $V_{\rm SW}$, and $\boldsymbol{B}_0$ is restricted to between 0° and 90°. This streaming speed is relative to the flow of the solar wind and is directed back toward the Sun. The solar wind carries the magnetic field lines about which the pickup ion gyrates with a radius of $\sim V_{\rm SW}\sin\theta_{VB}/(2\pi f_{i,c})$, where $f_{i,c}$ is the cyclotron frequency of the ion. The cyclotron frequency can be expressed as $f_{i,c} = q_i B/(2\pi M_i c)$, where q_i is the ion charge, B is the magnetic intensity, and c is the speed of light.

The newly ionized pickup ions form a ring-beam distribution that is resonantly unstable to waves (M. A. Lee & W.-H. Ip 1987). For the inner heliosphere, θ_{BV} is generally less than 70°. With these angles, fast waves are cyclotron resonant with species i in accord with $\omega + k_\parallel V_{\rm SW}\cos\theta_{BV} = -2\pi f_{i,c}$, where ω is the wave frequency, and $k_\parallel$ is the wavevector component along $\boldsymbol{B}_0$. Fast waves traveling sunward are unstable with maximum growth rate for parallel propagation. The wave frequency of the lowest magnitude of $k_\parallel$ has $\omega \approx kV_{\rm A}$, where $V_{\rm A}$ is the Alfvén speed. At 1 au, $V_{\rm SW}$ is much larger than $V_{\rm A}$. The minimum magnitude $|k_{\parallel,i}|$ for species i or equivalently the longest wavelength $\lambda_{\parallel,i}$ can be estimated from the resonant condition to be $\lambda_{\parallel,i} \lesssim V_{\rm SW}\cos\theta_{BV}/f_{i,c}$, where the inequality corresponds to fast waves with wavelengths as long as $\lambda_{\parallel,i}$ and shorter.

The speed of the waves and the speed of Solar Orbiter at 1 au are significantly less than $V_{\rm SW}$. Turbulent fluctuations also have a rate of change due to nonlinear evolution that is small compared with the rate that fluctuations are advected by the solar wind past the spacecraft. As a result, wave and turbulent fluctuations can be considered, approximately, to be frozen into the flow and simply advected past the spacecraft. This assumption, as applied to turbulence, is called the Taylor hypothesis (G. I. Taylor 1938). In this limit, the advection of the fluctuations past the spacecraft allows the time of transit to be transformed into the spatial extent of the fluctuations along the direction of the wind or vice versa. Generally, the solar wind flows along the radial direction, and θ_{BV} is approximated as the angle θ_{BR} between $\boldsymbol{B}_0$ and the radial direction. The pickup waves in the spacecraft frame have $\lambda_{\parallel,i}$ projected along the radial direction as $\lambda_{R,i} \lesssim V_{\rm SW}/f_{i,c}$ where the radial wavelength $\lambda_{R,i}$ is $\lambda_{\parallel,i}/\cos\theta_{BR}$. In terms of the spacecraft frame frequency f, pickup ion waves are found to begin where $f \gtrsim f_{i,c}$ for each species i and extend up to higher frequencies.

The O^+ ions in the present analysis develop waves near $f = 3 \times 10^{-3}$ Hz and He^+ waves at 4 times this value. As such, the detection of O^+ determines the lowest frequencies to be included in the spectrum and the interval duration. To provide enough neighboring frequencies to sample adequately about $f_{{\rm O},c}$, the interval durations used in the present analysis range from 1 to 2.4 hr so that the difference between frequencies Δf in the spectrum ranges from 2.7×10^{-4} to 1.2×10^{-4} Hz. These durations are also sufficient for the turbulent fluctuations, which have an expected correlation time of 30 minutes or more.

Waves from pickup ions must be detected amidst the turbulent fluctuations that pervade the interplanetary medium. With turbulence alone, the power spectrum toward higher f is organized by power-law ranges. At the lowest f is an energy-containing range with a power-law index near −1. Next at the higher f is an inertial range with a power-law index averaging −1.6 (C. W. Smith et al. 2006). In the turbulent inertial range, energy is cascaded from the energy-containing range and conserved from scale to scale toward kinetic scales. The pickup ion waves develop at frequencies corresponding to the inertial range (M. A. Lee & W.-H. Ip 1987). In the power spectrum, these waves contribute to a sharp rise in power at $f_{i,c}$, and then the excess power slowly falls back toward the slope originally followed by the turbulence-only spectrum at higher f. Next in order for the ranges is the ion dissipation range, beginning near 0.3 Hz in the spacecraft frame where the spectrum follows a steeper power law with indices between −2 and −4 (C. W. Smith et al. 2006; S. A. Markovskii et al. 2008). Here, fluctuating kinetic and magnetic energy of the turbulence is exchanged with ion thermal energy through collisionless fluctuation–particle interactions. Waves can also form in the ion dissipation range in association with proton thermal instabilities or shock-accelerated particles. They tend to form a rounded localized bump in power in this part of the spectrum. Such occurrences are observed in about 4% of all spectra obtained near 1 au (S. A. Markovskii & B. J. Vasquez 2022). Still higher f are electron ranges, but outside of aliasing, these are not observed directly by Solar Orbiter due to the cadence limit of the magnetometer employed.

The search for waves from pickup ions uses two magnetic field spectral techniques (B. E. Cannon et al. 2014a, 2014b; M. R. Argall et al. 2015, 2017; P. Aggarwal et al. 2016; M. K. Fisher et al. 2016; S. J. Hollick et al. 2018a, 2018b; A. V. Marchuk et al. 2021; L. Ercoline et al. 2023). First, the fluctuation power spectrum itself is obtained following the Blackman–Tukey approach (R. B. Blackman & J. W. Tukey 1958). Second, Fourier spectral and minimum variance analyses are applied, which determine minimum variance direction and polarization properties of the fluctuations as a function of spacecraft frequency.

Prior to calculating the spectrum, an automated search for outliers is made in each magnetic field component in the candidate interval. At the first stage, the entire interval considered for a spectrum is examined, and points that are 3.5 standard deviations from the average are flagged. A second pass in blocks of 2000 points is made, and points at 2.5 standard deviations from the average are flagged. Typically, less than 1% of the data are found to be flagged.

Any flagged points are excluded directly by the Blackman–Tukey algorithm (R. B. Blackman & J. W. Tukey 1958; J. W. Bieber et al. 1993). Spectra computed with this algorithm give the Fourier transform of the correlation tensor of the magnetic field $\langle B_i B_j \rangle$. The data are then prewhitened by a first-order difference filter and postdarkened on output (J. Chen 1989) to correct for power leakage in a sharply decreasing spectrum typical of the turbulence kinetic range. The power spectrum is derived from the trace of the diagonal components of the tensor.

The polarization spectra are computed with a fast Fourier transform of the time series (R. A. Fowler et al. 1967; J. D. Means 1970; D. Rankin & R. Kurtz 1970; W. H. Mish et al. 1982). With the Fourier transform, evenly spaced samples are required, and so any flagged data from the outlier search will be filled by interpolation. The fast Fourier transform method gives a power spectrum that agrees with the spectrum from the Blackman–Tukey method, but the effect of power leakage is greater. A spectral tensor $\langle \tilde{B}_i \tilde{B}_j^* \rangle$ is formed where $\tilde{B}_i$ is the Fourier transform of the ith component of the magnetic field, and $\tilde{B}_j^*$ is the complex conjugate of the transform. The spectral tensor elements are then smoothed over 15 frequencies centered about each f in the spectrum, except near the low and high end of the spectrum's range. The minimum variance direction is then calculated for each f to represent the wavevector $\boldsymbol{k}$. Generated pickup ion waves with the largest growth rates propagate along $\boldsymbol{B}_0$, and in the data, $\boldsymbol{k}$ would be expected to have an oblique angle less than 15°. The spectral tensor is then rotated into the minimum variance coordinate system with one axis along $\boldsymbol{k}$ and the other two in the plane transverse to $\boldsymbol{k}$. It is in this transverse plane that properties of any waves are sought.

One of these properties is the ellipticity. The ellipticity $E_{\rm lip}$ is the ratio of the minimum to maximum axes of the fluctuation ellipse in the plane perpendicular to $\boldsymbol{k}$. The value of $E_{\rm lip}$ can vary between -1 and 1. Right-hand polarization is assigned for $E_{\rm lip} > 0$ and left-hand for $E_{\rm lip} < 0$ in the spacecraft frame. The magnitude $|E_{\rm lip}|$ corresponds to linear polarization when $|E_{\rm lip}| = 0$, circular polarization when $|E_{\rm lip}| = 1$, and elliptical polarization for intermediate values. Detected pickup ion waves for some range of f generally have $|E_{\rm lip}|$ exceeding 0.5. Since the waves are fast modes traveling sunward, they are left-handed in the spacecraft frame. Interplanetary turbulent fluctuations generally have no net ellipticity at the frequencies where pickup ion waves develop.

Coherence and degree of polarization are also calculated. These vary between 0 and 1. A coherent signal toward 1 is expected when the waves are well identified and the degree of polarization is near 1 when the fluctuating component of the magnetic field is small along the direction of $\boldsymbol{k}$. Where $|E_{\rm lip}|$ is large over some range of f for pickup ion waves, so usually are the coherence and degree of polarization. Generally, ellipticity of the proper sign, magnitude, and frequency range is used to find a candidate pickup ion wave interval. It is then determined if there is an elevation of power at these frequencies and that the waves have $\boldsymbol{k}$ with a small obliquity. Coherence and degree of polarization are usually also significant when all three of the above conditions are satisfied. Hence, coherence and degree of polarization are secondary indicators for waves.

The above second technique gives the primary identification of quasi-parallel waves predicted to be excited by pickup ions as they scatter from newly ionized ions in a ring beam. Waves driven by pickup ions of a particular species occur at its cyclotron frequency and higher in the spacecraft frame. The first technique confirms, to the extent possible with magnetic fields alone, the presence of these waves as an elevation above the turbulent spectrum that sharply rises near $f_{i,c}$ in the spacecraft frame and slowly descends toward the turbulent power-law spectrum at higher f. The values of $f_{{\rm He},c}$ and $f_{{\rm O},c}$ differ by a factor of 4. In the case of interstellar protons, waves associated with both H^+ and He^+ pickup ions are observed in the outer heliosphere. The same spectral analysis techniques have distinguished the generated waves from each ion when both waves are present. In this case, a factor of 4 in frequency also separates these species.

The HIS instrument provides important constraints on wave identification: it determines whether or not the ions are present during the intervals examined for spectra and gives an indication of the potential pickup ion wave intensity for different ions relative to each other.

3. Results

The proximity of the ion tail of Comet Leonard can be identified by the increased presence of O^+ as measured by Solar Orbiter. Figures 1(a)–(g) present hourly plasma and magnetic field data during the time of passage through the comet tail. Figures 1(a) and (b) display (a) counts attributed to O^+ as a function of time and (b) the counts per hour as functions of time and E/Q. A similar set of plots is given by He^+ in panels (c) and (d). Figures 1(e) and (f) show (e) the magnetic field strength B and components of $\boldsymbol{B}$ and (f) the angle θ_{BR} between $\boldsymbol{B}$ and the radial direction as functions of time. The last panel, Figure 1(g), plots the proton speed $V_{\rm SW}$ and number density $n_{\rm p}$. The interval extends from 2021 December 16 through 2021 December 18. There is a plasma data gap between December 16 21 UTC and December 17

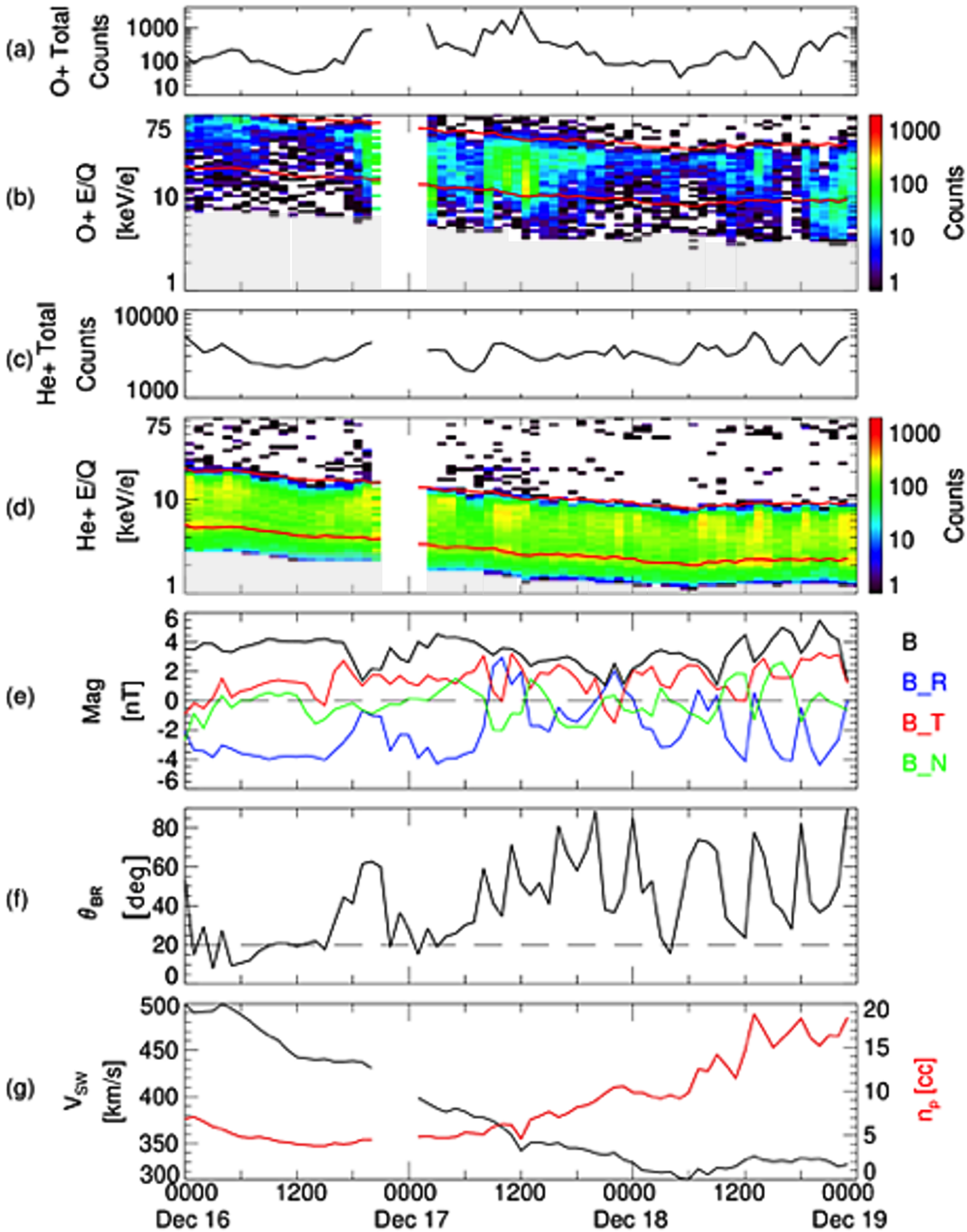

Figure 1. Hourly in situ data from 2021 December 16 to 18. (a) Total plotted counts attributed to O^+ as a function of time and (b) O^+ counts as functions of time and energy per charge (E/Q). (c) Total plotted counts for He^+ as a function of time and (d) He^+ counts as functions of time and E/Q. (e) Magnetic field B (black), B_R (blue), B_T (red), and B_N (green), (f) θ_{BR}, and (g) $V_{\rm SW}$ (black) and $n_{\rm p}$ (red) as functions of time. The red lines in panels (b) and (d) correspond to the ion moving at $V_{\rm SW}$, and the gray-shaded areas are filtered by a cutoff speed. The dashed line in panel (f) has $\theta_{BR} = 20°$.

2 UTC. Preceding and following this time interval are solar ejecta that are excluded from this study. During this time, the spacecraft was located near 1 au.

In total counts, the distribution of O^+ in Figure 1(a) has a moderately uniform component with about 100 counts along with episodic bursts of high concentrations up to 3000 counts that occur between 930 UTC and 1230 UTC on 2021 December 17. There is also a significant increase preceding and a decrease following the five-hour data gap, which cannot be fully investigated. The high concentrations can result from the outgassing of material from spatially confined jets located on the nucleus of Comet Leonard, possibly during outbursts. This part of the tail is viewed as a central place where the plasma has followed a streamline directly from the nucleus. The more uniform region corresponds to the dispersal of jet material and other sources of sublimation of icy material on the nucleus into a space-filling coma about the nucleus. The ionization of the coma material then contributes to the ion tail.

There are interstellar O^+ ions, but these have a very low relative abundance (C. Drews et al. 2012). Generally, very few such ions would be counted in the whole three-day interval. Pickup O^+ ions can also come from O ions interacting with dust grains in the inner solar system, which is the so-called inner source (R. F. Wimmer-Schweingruber & P. Bochsler 2003; P. R. Quinn et al. 2018). The inner source O^+ ions have been analyzed by HIS in fast winds ($V_{SW} > 500$ km s^{-1}) with amounts that are 2 orders of magnitude smaller than observed in this three-day interval. In slow winds, an analysis of HIS has not been performed that can definitively determine the amount of the inner source O^+ ions apart from background contaminants. Leonard (see Figure 1(g)) occurs during a slow wind interval. Likely the amounts of inner source O^+ ions in such an interval would also be well below what is observed for Leonard. Thus, the observed O^+ ions are expected to originate mostly from the comet.

Pickup ions injected at low speeds with respect to the solar wind will exhibit speeds up to $2V_{SW}$ when fully scattered. Relying on this property, the O^+ distribution in Figure 1(b) is cut off at speeds below $0.6V_{SW}$ (the gray-shaded region) to limit the contribution from accidental time-of-flight coincidences, which occur most often near the E/Q peaks for solar wind protons and alphas and cause spurious M/Q counts (S. Livi et al. 2023). Below the energy associated with this speed, no counts for O^+ are plotted or recorded in the counts shown in panel (a). The plotted red line is the energy of O^+ with speed V_{SW}. At higher energies, an approximate upper-limiting boundary forms for O^+ with speeds near $2V_{SW}$. Near 6 UTC on December 16, when V_{SW} is near 500 km s^{-1}, the concentration of O^+ on the upper boundary is most evident apart from the outbursts. Even so, features along this boundary can be traced throughout the interval as the V_{SW} decreases with time, and outburst periods are sharply limited along this boundary. The distribution of ions in association with $2V_{SW}$ results from the injection of O^+ at low speeds near the comet, which drive unstable waves that have thoroughly scattered up the ions across an approximate spherical shell in the wave–particle frame that is centered about the speed of the wind so that at minimum the speed is near 0 and at maximum the speed is near $2V_{SW}$ because energy is conserved in this frame.

Figure 1(c) plots counts per hour attributed to He^+ in the same manner as in Figure 1(a). At all times, the total counts are high, with an average near 3000. This distribution corresponds to the broad distribution of He^+ in the focusing cone that extends about $\pm 15°$ in ecliptic longitude about its central axis. During the three-day interval, Solar Orbiter on average was 0°7 above the ecliptic plane and at a solar ecliptic longitude of 79°. Solar Orbiter made its closest approach to the inferred axis of the focusing cone on December 12 at a longitude of 75°4 (S. A. Spitzer et al. 2024). The counts of He^+ far exceed the background level of O^+ counts, even when accounting for the heavier mass difference. At maximum concentration, though, O^+ counts do become comparable to He^+.

Comet Leonard does not appear to contribute to the observed He^+ ions. There are no variations associated with outburst periods as there are in O^+ counts. The distribution of He^+ is not found to be enhanced inside compared to outside of the three-day comet interval. Likely Comet Leonard is not a source of He^+.

Figure 1(d) shows that the energy per charge distribution of He^+ is relatively uniform with time. Low energies are cut off in association with speeds of $0.8V_{SW}$ to remove time-of-flight coincidences from originating from high fluxes of solar wind protons and alphas. Additional culling has been done using energy measurements from the solid-state detectors to determine mass separately from charge, but some mixing with ions other than interstellar He^+ may be occurring for ions with speeds below $1.3V_{SW}$. The plotted red line corresponds to He^+ with speed V_{SW}. Again, there is an upper boundary associated with $2V_{SW}$. Pickup He^+ can be derived from interstellar neutrals and potentially from interactions between He^{2+} from the Sun interacting with interplanetary dust particles (again referred to as the inner source) (R. F. Wimmer-Schweingruber & P. Bochsler 2003; P. R. Quinn et al. 2018). Pickup ions from interstellar neutrals are injected at low speeds relative to the solar wind and have particle velocity space distributions that are unstable to waves. The observed upper boundary near $2V_{SW}$ is consistent with low-speed injection. The interactions involving dust can proceed by different mechanisms whose relative occurrence in the solar wind is not yet specified. The generation of waves from these mechanisms is not definitively known. Moreover, since the spacecraft is in the He^+ focusing cone associated with the interstellar source, it is likely that a significant fraction of He^+, if not most, is derived from interstellar neutrals. From here on out, any He^+-associated waves will be ascribed to the interstellar source without further comment.

Figures 1(e) and (f) present hourly magnetic field conditions for the interval. Panel (e) shows the magnetic field intensity B (black) and components. The radial magnetic field B_R is the blue line, tangential B_T red, and normal B_N green. Panel (f) plots the oblique angle θ_{BR} between $\boldsymbol{B}$ and the radial direction. The last panel (g) gives the proton solar wind speed V_{SW} and shows the proton number density n_p. The hourly data for the magnetic field are complete, whereas the thermal proton data have the same five-hour data gap as the O^+ and He^+ data.

In Figure 1(e), B_R turns from inward to outward and then back again between December 17 900 UTC and 1300 UTC. This indicates the presence of large current sheet crossings. Just before, the plasma data gap B_R approached 0 but never completely turned. After December 17 1300 UTC, smaller excursions of short duration occur across zero. At times, the direction of $\boldsymbol{B}$ is within about 20° of the radial direction. A prolonged period occurs on December 16 from 2 UTC to 16 UTC. Another period with θ_{BR} near 20° occurs between

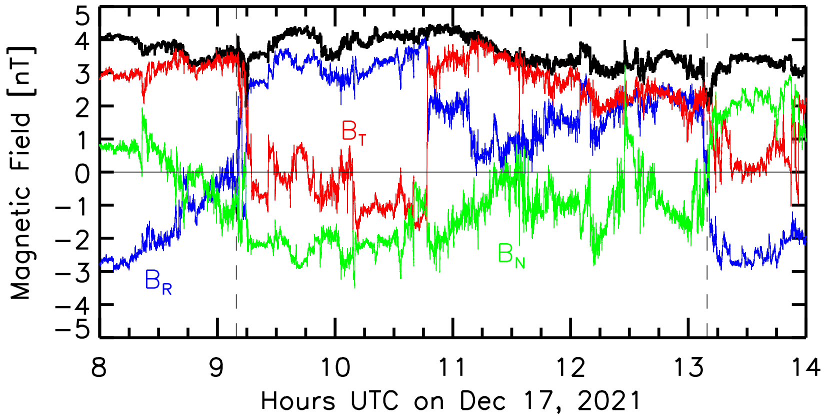

Figure 2. Plot of magnetic fields at the perceived center of the ion tail using data at eight vectors per second. The values of B (black), B_R (blue), B_T (red), and B_N (green) are shown as a function of time.

December 16 22 UTC and December 17 4 UTC, but is partially in the plasma data gap. On December 18, the field direction only once and briefly approaches the radial direction. The solar wind mainly has a declining speed through the interval from 500 to 325 km s^{-1}. The density decreases up to December 16 12 UTC, corresponding to a rarefaction region as the slower wind falls behind the faster wind. In the rarefaction, proton number flux ($n_p V_{SW}$) is not conserved as the rarefaction is not a steady flow in the inertial frame of the Sun. This can contribute to $\boldsymbol{B}$ turning into the radial direction. At later times, n_p increases significantly. This is a compression region where $\boldsymbol{B}$ is more oblique.

The perceived center of the ion tail corresponds to a region between the two large current sheets where the B_R changes from inward to outward and back again, marked by the vertical dashed lines. The change in B_R as opposed to the other components is used here because a comet drapes the interplanetary magnetic field about itself and causes the directional sense of the magnetic field to change orientation with respect to the direction with the Sun. Figure 2 shows the magnetic fields in this vicinity between December 17 8 UTC and 14 UTC with a cadence of eight vectors per second. The current sheets occur at about 910 UTC and 1310 UTC. In Figure 1(a), the episodic and high concentrations of O^+ occur between these two sheets. With V_{SW} near 350 km s^{-1}, the transit time of the plasma from the comet is about 32 hr. The magnetic field structure in this portion of the tail is likely explained by the draping of the magnetic field about Comet Leonard. In contrast, the potentially high-concentration region of O^+ about the data gap is not bound by current sheets. All components of $\boldsymbol{B}$ around and within this region show fluctuations of short scales that ride along with the larger-scale variations of $\boldsymbol{B}$. The magnetic intensity is not constant and varies irregularly, decreasing from about 4 nT at 8 UTC to 3 nT at 14 UTC. Many of these smaller-scale fluctuations correspond with turbulence that pervades the entire three-day interval.

Waves associated with the He^+ cyclotron frequency $f_{He,c}$ in the spacecraft frame are found on December 16 in three intervals with durations of 2.4 hr. They are not found on December 17 or 18. Table 1 gives the start and stop times of these intervals. All times for the waves correspond to the prolonged period of the quasi-radial magnetic field. Two spectra overlap by 50%. The better wave signature of the two is shown in Figure 3 with a start time of 1048 UTC. In the top panel, the magnetic field spectrum of the trace of the components is given. The spectrum has a power-law form. A small but distinct elevation in power over and above the general trend of the power law from lower f is found at $f_{He,c}$ and extends back toward the proton cyclotron frequency $f_{p,c}$. This portion of the spectrum corresponds to the turbulent inertial range. In this frequency range, the fourth panel from the top shows a consistent negative ellipticity whose magnitude exceeds 0.5. The negative ellipticity values correspond to left-hand polarized waves in the spacecraft frame, as is expected for waves generated by a ring-beam instability associated with interstellar pickup ions. The last panel shows the obliquity of the wavevector direction, which is nearly along $\boldsymbol{B}_0$. Waves growing from pickup ions should be most prevalent in this direction. Following these key signatures, the degree of polarization in the second panel from the top and the coherence in the third are both above 0.5 in the same frequency range.

Table 1
Times on 2021 December 16 when Spectra with He^+ Waves Were Found

Start	Stop
712 UTC	936 UTC
1048 UTC	1312 UTC
1200 UTC	1424 UTC

A further wave interval (not shown) featured He^+ waves with a similar intensity and also a strong bump in power at frequencies higher than $f_{p,c}$. The higher frequency signature corresponds to quasi-parallel waves likely driven by some thermal plasma instability. Solar Orbiter did not encounter a shock in this interval.

Despite the detection of He^+ waves in these intervals and the likelihood that generated quasi-parallel waves of any source would be favorable to observe, no waves were detected at the O^+ cyclotron frequency $f_{O,c}$. A search of the entire 3 days found no occurrence of these waves. Special attention was paid to the intervals within the large current sheets where O^+ is highly concentrated at times. Spectra for the key signatures of the ring-beam instability were examined at various interval durations and overlapping of intervals. These signatures were not identified. The possibility of pickup ion-generated waves resulting from an instability due to the

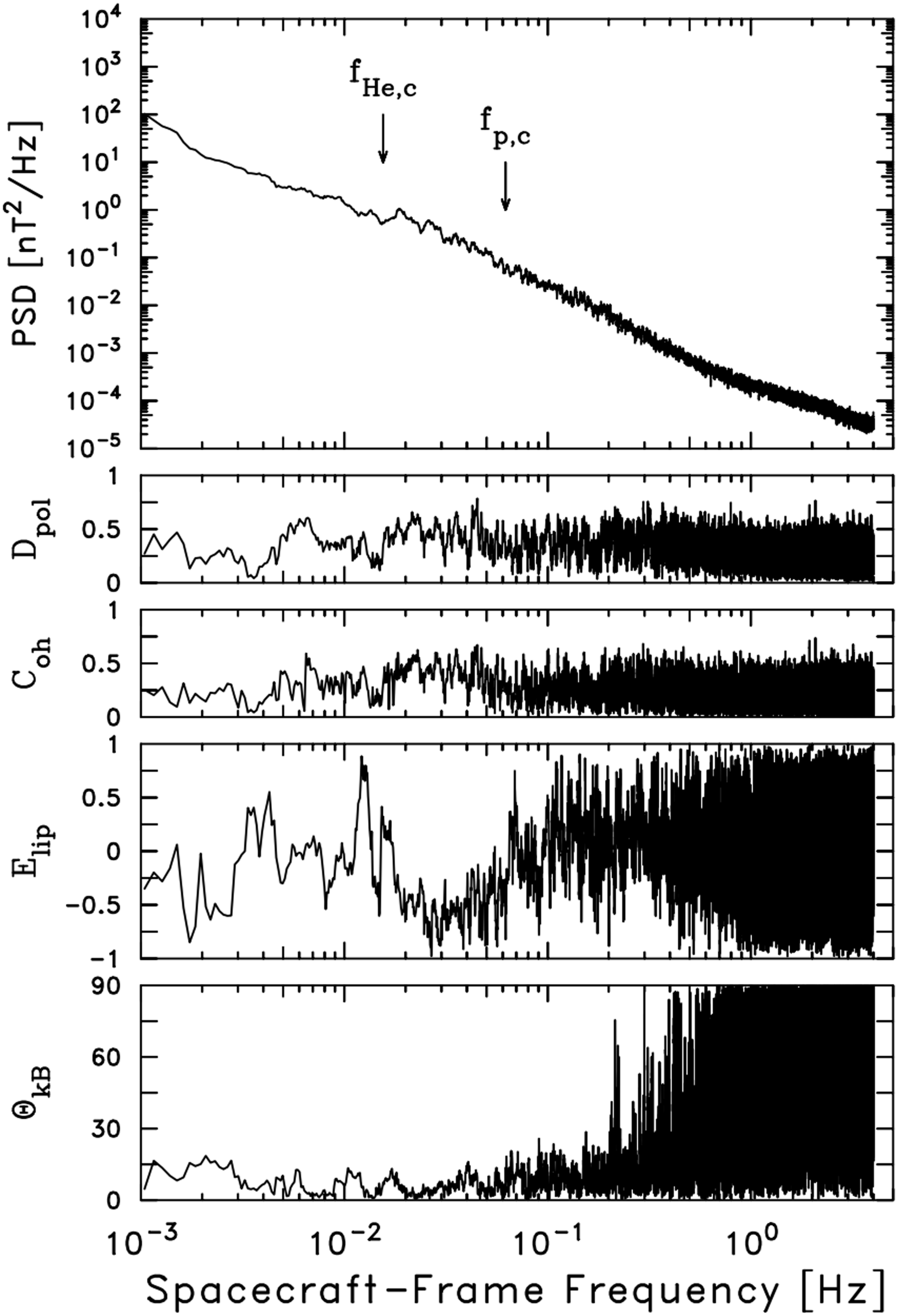

Figure 3. Plot of a He^+ wave interval. The top panel is the magnetic field power spectrum as a function of spacecraft frequency. Successive panels display the degree of polarization, coherence, ellipticity, and the oblique angle between the minimum variance direction and $\boldsymbol{B}_0$. The lowest spacecraft frequencies in the spectrum are not shown.

inhomogeneous concentrations of O^+ associated with jets from the comet nucleus was also examined (L. Matteini et al. 2021). These waves would be linearly polarized. In this case, an elevation of power at $f_{\mathrm{He},c}$ would be expected but with no ellipticity differing consistently from 0. These signatures were also not found.

4. Discussion

Pickup He^+ waves are visible earlier in the three-day interval where V_{SW} is declining but not later when speeds are low and relatively unchanging. The plasma and magnetic fields in the declining speed region are subject to rarefaction. The background magnetic field $\boldsymbol{B}_0$ lines are turned closer to the radial sampling direction than Parker spiral magnetic field lines would with equivalent V_{SW}. In contrast, the following slow wind region has prolonged intervals where $\boldsymbol{B}_0$ has an average obliquity of about 45°. This same magnetic field orientation occurs at the perceived center of the ion tail as well as in the immediate surroundings and in the farther following region.

The ring-beam instability drives waves that are most intense for those propagating along $\boldsymbol{B}_0$. The turbulent cascade generates fluctuations with wavevectors concentrated in directions perpendicular to $\boldsymbol{B}_0$. As $\boldsymbol{B}_0$ turns toward the radial direction, the waves become increasingly better seen because the quasi-perpendicular wavevectors of the turbulent fluctuations project to the sampling direction from larger wavenumbers, where the turbulent amplitude is smaller. In this case, the observed waves can stand out better amidst the turbulent fluctuations and have greater potential visibility. The reverse is true as $\boldsymbol{B}_0$ turns away from the radial direction.

Another factor to consider is the competition between the generation of the He^+ waves and turbulence. In the focusing cone, newly ionized He^+ is sustained over long times by the inflow of interstellar neutrals and their interaction with EUV photons from the Sun and, to a lesser degree, by their interaction with electrons. Since He^+ is distributed nearly continuously throughout the focusing cone, waves should form throughout the focusing cone and even beyond.

Turbulent fluctuations participate in an energy cascade from large to small scales where energy dissipates. Quasi-parallel waves can be consumed in this process due to nonlinear interactions with quasi-perpendicular fluctuations that transfer quasi-parallel wave power into fluctuations with more oblique wavevectors where the energy is eventually dissipated (J. V. Shebalin et al. 1983; S. Oughton et al. 1994). Large statistical studies of interstellar pickup ion waves find that rarefactions often show the waves and have turbulent fluctuations with smaller amplitudes and so smaller cascade rates than elsewhere (B. E. Cannon et al. 2014a, 2014b; S. J. Hollick et al. 2018a, 2018b; A. V. Marchuk et al. 2021; L. Ercoline et al. 2023). Model calculations comparing expected wave production rates for pickup ions with turbulence cascade rates find that the wave production rates generally exceed the cascade rates where the waves are observed (B. E. Cannon et al. 2014a, 2014b; S. J. Hollick et al. 2018a, 2018b; A. V. Marchuk et al. 2021; L. Ercoline et al. 2023). Much of this work has been done for conditions at 3 au and outward.

Near the Sun, turbulent amplitudes are larger and decrease with increasing heliocentric distance r. The cascade rate decreases as $r^{-3/2}$ (B. J. Vasquez et al. 2007). The ability of turbulence to overcome the production of waves in the inner heliosphere is likely significant and could account for the rare observation of pickup ion waves near 1 au (M. R. Argall et al. 2015; M. K. Fisher et al. 2016).

Pickup O^+ waves from Comet Leonard were not detected in the present analysis, even in intervals where He^+ waves were observed. Two factors stand out as possible reasons for the lack of detection. First, at the fourfold lower frequency for O^+ waves than He^+ waves to form, the fluctuating magnetic field power in a Kolmogorov-like inertial range ($f^{-5/3}$) is 9 times larger at $f_{\mathrm{O},c}$ than at $f_{\mathrm{He},c}$. Thus, for any waves at $f_{\mathrm{O},c}$ to match the elevation of wave power at $f_{\mathrm{He},c}$, 9 times the intensity would be required. Lastly, an instability associated with O^+ is not sustained as the instability for He^+ is. Most of the water molecules released from the nucleus that disassociate into oxygen and ionize do so within ∼0.01 au of the nucleus (P. W. Daly 1991). As long as newly ionized O^+ is produced, waves can be driven. Eventually, this reserve is diminished to the point that there are no newly ionized particles. At this point, the accumulated wave energy cannot be further enhanced. This condition is met close to the comet nucleus. Thereafter, any cometary waves observed far from the nucleus must be transported with the interplanetary magnetic field imbedded in the solar wind to reach a spacecraft positioned in a distant portion of the comet's tail. With no additional wave power accumulation, only processes that cause wave power loss operate during the transport to the spacecraft. With an active turbulent cascade among the magnetic field and velocity fluctuations accompanying the O^+, such loss is expected. This would limit the visibility of the waves in the power spectrum and ultimately dissipate the wave energy.

Finally, it should be noted that the activity of Comet Leonard complicates analysis. Up until about December 13, it had a fairly consistent gas output. Thereafter, it underwent outbursts, and changes in the tail itself occurred. As such, the comet was not a steady source of pickup ions, and the tail was not a regular structure at all times. This could influence the nature of O^+ waves from the comet in ways that cannot be fully understood with this analysis.

5. Summary

Solar Orbiter passed through Comet Leonard's tail while immersed well within the He^+ focusing cone. The nucleus of the comet was about 0.25 au from the spacecraft. A search for pickup ion waves associated with interstellar He^+ and cometary O^+ ions was made. Magnetic field spectra in a few intervals showed waves with signatures consistent with He^+. These same intervals did not show O^+ waves even though quasi-parallel waves should have been easier to find in such intervals. Waves associated with O^+ were not found in any of the 3 days considered in the present analysis.

In the inner heliosphere, the generation of pickup ion waves is a secondary process compared with turbulence and stream interactions. In the outer heliosphere, the roles reverse. At present, there are no reliable forecast methods to predict where ion pickup waves should be observable. Direct evidence of the pickup ion wave generation process in the inner heliosphere is scant. Some guidance is found from the tendency to identify waves in intervals where $\boldsymbol{B}_0$ is nearly in the radial direction and in rarefaction regions where turbulent amplitudes tend to be smaller than elsewhere. Cometary pickup ion waves are an exception and do stand out in regions within and near the comet coma, where the local plasma is mass loaded and altered with respect to average interplanetary conditions (B. T. Tsurutani 1991). Yet, far away from the comet, interplanetary turbulence should become a significant limiting factor on their visibility. Turbulence imposes a detection limit because the waves need to be intense enough to stand out amidst the turbulent fluctuations. For a fixed wave intensity, the visibility decreases at lower frequencies because the intensity of the turbulent fluctuations increases with decreasing frequency. As such, pickup O^+ generates lower frequency waves that are more obscured than the pickup He^+ waves.

Acknowledgments

Solar Orbiter is a mission of international cooperation between ESA and NASA, operated by ESA. Funding for SwRI was provided by NASA contract NNG10EK25C. Funding at the University of New Hampshire was provided through SwRI subcontract A99200MO. Funding for the University of Michigan was provided through SwRI subcontract A99201MO. P.L. thanks CNES for science support. B.L.A. acknowledges Solar Orbiter funding at NASA/GSFC.

ORCID iDs

Bernard J. Vasquez https://orcid.org/0000-0001-8593-7289
Charles W. Smith https://orcid.org/0000-0002-5379-1542
Antoinette Galvin https://orcid.org/0000-0003-3752-5700
Timothy J. Stubbs https://orcid.org/0000-0002-5524-645X
C. J. Owen https://orcid.org/0000-0002-5982-4667
S. Livi https://orcid.org/0000-0002-4149-7311
S. T. Lepri https://orcid.org/0000-0003-1611-227X
R. M. Dewey https://orcid.org/0000-0003-4437-0698
B. L. Alterman https://orcid.org/0000-0001-6673-3432
Yeimy J. Rivera https://orcid.org/0000-0002-8748-2123

References

Aggarwal, P., Taylor, D. K., Smith, C. W., et al. 2016, ApJ, 822, 94
Argall, M. R., Fisher, M. K., Joyce, C. J., et al. 2015, GeoRL, 42, 9617
Argall, M. R., Hollick, S. J., Pine, Z. B., et al. 2017, ApJ, 849, 61
Bieber, J. W., Chen, J., Matthaeus, W. H., Smith, C. W., & Pomerantz, M. A. 1993, JGR, 98, 3585
Biver, N., Bockelée-Morvan, D., Handzlik, B., et al. 2024, A&A, 690, A271
Blackman, R. B., & Tukey, J. W. 1958, The Measurement of Power Spectra (Dover Publications)
Cannon, B. E., Smith, C. W., Isenberg, P. A., et al. 2014a, ApJ, 784, 150
Cannon, B. E., Smith, C. W., Isenberg, P. A., et al. 2014b, ApJ, 787, 133
Chen, J. 1989, PhD thesis, Univ. Delaware, Newark
Daly, P. W. 1991, GMS, 61, 341
Drews, C., Berger, L., Wimmer-Schweingruber, R. F., et al. 2012, JGR, 117, A09106
Ercoline, L., Smith, C. W., Argall, M. R., et al. 2023, ApJ, 945, 168
Faggi, S., Lippi, M., Mumma, M. J., et al. 2023, PSJ, 4, 8
Fisher, M. K., Argall, M. R., Joyce, C. J., et al. 2016, ApJ, 830, 47
Fowler, R. A., Kotick, B. J., & Elliott, R. D. 1967, JGR, 72, 2871
Gershman, D. J., Gloeckler, G., Gilbert, J. A., et al. 2013, JGR, 118, 1389
Hollick, S. J., Smith, C. W., Pine, Z. B., et al. 2018a, ApJ, 863, 75
Hollick, S. J., Smith, C. W., Pine, Z. B., et al. 2018b, ApJ, 863, 76
Horbury, T. S., O'Brien, H., Blazquez, I. C., et al. 2020, A&A, 642, A9
Jewitt, D., Kim, Y., Mattiazzo, M., et al. 2023, AJ, 165, 122
Lee, M. A., & Ip, W.-H. 1987, JGR, 92, 11,041
Livi, S., Lepri, S. T., Raines, J. M., et al. 2023, A&A, 676, A36
Marchuk, A. V., Smith, C. W., Watson, A. S., et al. 2021, ApJ, 923, 185
Markovskii, S. A., & Vasquez, B. J. 2022, ApJ, 941, 72
Markovskii, S. A., Vasquez, B. J., & Smith, C. W. 2008, ApJ, 675, 1576
Matteini, L., Laker, R., Horbury, T., et al. 2021, A&A, 656, A39
Means, J. D. 1970, JGR, 77, 5551
Mish, W. H., Wenger, R. M., Behannon, K. W., & Byrnes, J. B. 1982, Interactive Dig- digital Signal Processor, NASA Technical Memorandum 83997, Goddard Space Flight Center, Greenbelt, MD. (Revised 1984.)
Oughton, S., Priest, E. R., & Matthaeus, W. H. 1994, JFM, 280, 95
Owen, C. J., Bruno, R., Livi, S., et al. 2020, A&A, 642, A16
Quinn, P. R., Schwadron, N. A., Möbius, E., et al. 2018, ApJ, 861, 98
Rankin, D., & Kurtz, R. 1970, JGR, 75, 5444
Shebalin, J. V., Matthaeus, W. H., & Montgomery, D. 1983, JPlPh, 29, 525
Smith, C. W., Hamilton, K., Vasquez, B. J., & Leamon, R. J. 2006, ApJL, 645, L85
Spitzer, S. A., Lepri, S. T., Raines, J. M., et al. 2024, ApJ, 974, 87
Taylor, G. I. 1938, RSPSA, 164, 476
Tsurutani, B. T. 1991, GMS, 61, 189
Vasquez, B. J., Smith, C. W., Hamilton, K., et al. 2007, JGR, 112, A07101
Watson, S. R., Scott, C. J., Owens, M. J., & Barnard, L. A. 2024, ApJ, 970, 101
Watson, S. R., Scott, C. J., Owens, M. J., Barnard, L. A., & Lang, M. 2025, ApJ, 982, 66
Wimmer-Schweingruber, R. F., & Bochsler, P. 2003, GeoRL, 30, 1077